


Article

Radiometric Cross-Calibration of HJ-2A/CCD3 Using the Random Forest Algorithm and a Spectral Interpolation Convolution Method with Sentinel-2/MSI

Xiang Zhou ¹, Yidan Chen ² , Yong Xie ², Jie Han ^{3,*} and Wen Shao ²

¹ College of Resources and Environment, University of Chinese Academy of Sciences, Beijing 100049, China; zhouxiang@aircas.ac.cn

² School of Geographical Sciences, Nanjing University of Information Science and Technology, Nanjing 210044, China; 202212110009@nuist.edu.cn (Y.C.); xieyong@nuist.edu.cn (Y.X.); wenshao@nuist.edu.cn (W.S.)

³ School of Geography and Geomatics, Xuchang University, Xuchang 461000, China

* Correspondence: hanjie@radi.ac.cn; Tel.: +86-374-2968710

Abstract: In the process of radiometric calibration, the corrections for bidirectional reflectance distribution functions (BRDFs) and spectral band adjustment factors (SBAFs) are crucial. Time-series MODIS images are commonly used to construct BRDFs by using the Ross–Li model in current research. However, the Ross–Li BRDF model is based on the linear relationship between the kernel models and is unable to take into account the nonlinear relationship between them. Furthermore, when using SBAF to account for spectral difference, a radiative transfer model is often used, but it requires many parameters to be set, which may introduce more errors and reduce the calibration accuracy. To address these issues, the random forest algorithm and a spectral interpolation convolution method using the Sentinel-2/multispectral instrument (MSI) are proposed in this study, in which the HuanJing-2A (HJ-2A)/charge-coupled device (CCD3) sensor is taken as an example, and the Dunhuang radiometric calibration site (DRCS) is used as a radiometric delivery platform. Firstly, a BRDF model by using the random forest algorithm of the DRCS is constructed using time-series MODIS images, which corrects the viewing geometry difference. Secondly, the BRDF correction coefficients, MSI reflectance, and relative spectral responses (RSRs) of CCD3 are used to correct the spectral differences. Finally, with the validation results, the maximum relative error between the calibration results of the proposed method and the official calibration coefficients (OCCs) published by the China Centre for Resources Satellite Data and Application (CRESDA) is 3.38%. When tested using the Baotou sandy site, the proposed method is better than the OCCs of the average relative errors calculated for all the bands except for the near-infrared (NIR) band, which has a larger error. Additionally, the effects of the light-matching method and the radiative transfer method, different approaches to constructing the BRDF model, using SBAF to account for spectral differences, different BRDF sources, as well as the imprecise viewing geometrical parameters, spectral interpolation method, and geometric positioning error, on the calibration results are analyzed. Results indicate that the cross-calibration coefficients obtained using the random forest algorithm and the proposed spectral interpolation method are more applicable to the CCD3; thus, they also account for the nonlinear relationships between the kernel models and reduce the error due to the radiative transfer model. The total uncertainty of the proposed method in all bands is less than 5.16%.

Keywords: HuanJing-2A (HJ-2A); Sentinel-2; cross-calibration; bidirectional reflectance distribution function (BRDF); random forest algorithm; spectral difference



Citation: Zhou, X.; Chen, Y.; Xie, Y.; Han, J.; Shao, W. Radiometric Cross-Calibration of HJ-2A/CCD3 Using the Random Forest Algorithm and a Spectral Interpolation Convolution Method with Sentinel-2/MSI. *Remote Sens.* **2024**, *16*, 4337. <https://doi.org/10.3390/rs16224337>

Academic Editors: Stefania Bonafoni and Yunbin Yuan

Received: 18 October 2024

Revised: 18 November 2024

Accepted: 19 November 2024

Published: 20 November 2024



Copyright: © 2024 by the authors. Licensee MDPI, Basel, Switzerland. This article is an open access article distributed under the terms and conditions of the Creative Commons Attribution (CC BY) license (<https://creativecommons.org/licenses/by/4.0/>).

1. Introduction

During a satellite's operation in orbit, the radiometric performance of its sensors may change due to variations in the surrounding environment and its motion dynamics [1].

Thus, performing timely radiometric calibration is essential for quantitative remote sensing research on satellite imagery, which is a prerequisite for ensuring the quality of data and products during the life cycle of a payload and represents the core and foundation of quantitative remote sensing [2]. This process not only enables the real-time monitoring of changes in the sensor's radiometric characteristics but also allows for the assessment of its radiometric quality, thereby strongly supporting the stability of remote sensing data [3].

Generally, radiometric calibration can be categorized into two broad types: absolute radiometric calibration and relative radiometric calibration [4,5]. Relative radiometric calibration is the process of correcting for differences in the relative response of the imaging elements of a sensor [6]. Absolute radiometric calibration establishes a quantitative relationship between the digital number (DN) of the image and the amount of radiation [7]. Absolute radiometric calibration has an important impact on the improvement in remote sensing image quality and applications [8,9], ensuring the reliability of image data and meeting the needs of quantitative applications [3].

Among the current commonly used absolute radiometric calibration methods in China are on-orbit calibration, site calibration, and cross-calibration [10–12]. However, no on-orbit calibrator systems have been installed on the many existing satellite platforms, which makes it infeasible to achieve on-orbit calibration. The China Center for Resources Satellite Data and Application (CRESDA) also conducts site calibration experiments only once a year in July–September, a process that is costly in terms of human, material, and financial resources and requires regular monitoring [3,13,14]. Cross-calibration has become widely utilized over the years because of its low cost, high frequency, and high accuracy [15,16]. For example, Xie et al. [17] developed the bottom-of-atmosphere (BOA) and the top-of-atmosphere (TOA) spectral band adjustment factor (SBAF) model using the Sentinel-3/ocean and land color instrument sensor to correct for differences in sensor spectra with the HaiYang-1C/Chinese ocean color and temperature scanner (COCTS) sensor. The results indicate that the BOA SBAF is more effective for cross-calibration of the COCTS. To overcome the problems caused by the large field of view of satellites, Dong et al. [18] proposed a cross-calibration scheme using the combined observation data of Gaofen-1 (GF-1) and GF-6, thus expanding their applicability to various viewing geometries. Han et al. [19] used the bidirectional reflectance distribution function (BRDF) parameters and SBAF parameters to correct the spectral and geometric differences between the GF-4/panchromatic and multispectral sensors and the Landsat8/operational land imager, finally obtaining the cross-calibration coefficients. Using GF-5/advanced hyperspectral images, which offer better calibration performance, cross-calibration is adopted by Niu et al. [20] to calibrate the Ziyuan1-02D. Using a Moderate-Resolution Imaging Spectroradiometer (MODIS) to construct a BOA BRDF model and the cubic polynomial interpolation approach, Han and Tao [21] provided an ideal cross-calibration project for a GF-6/wide-field-of-view sensor in case of a lack of reference bands. Liu et al. [22] utilized the MODIS sensor to correct spectral differences with the HuanJing-1A (HJ-1A)/charge-coupled device (CCD1), successfully completed cross-calibration of the CCD1 sensor, and investigated its on-orbit operational performance.

In previous studies, the viewing geometric differences between sensors are often corrected by BRDF, and time-series MODIS images are often used for constructing the BRDF model by Ross–Li [19,22,23], which is used to obtain the BRDF correction coefficients. On the other hand, when considering the spectral difference between two sensors, it is common to use SBAF for correction, which requires the simultaneous measurement of surface parameters and atmospheric parameters, followed by spectral correction using a radiative transfer model; the surface reflectance is then simulated to the TOA reflectance [12,17,21]. Currently, there are two major issues that require further research and implementation.

- The traditional Ross–Li BRDF model is based on the linear relationship between the kernel models, and the nonlinear relationship fails to adequately consider.
- The measured data are often difficult to obtain, especially when carrying out historical data calibrations using SBAF to correct spectral differences. Although Han et al. [15]

proposed an interpolation method using MOD09GA instead of measured data, the radiative transfer model also causes an increase in the uncertainty of the calibration results [10,24].

Therefore, this study takes the HJ-2A/CCD3 sensor as an example, choosing Sentinel-2/MSI as a reference sensor, and builds a BRDF model by using the random forest algorithm with time-series MODIS images. Then, the method for constructing the BRDF model that is more suitable for CCD3 is further explored. In addition, we interpolate the TOA reflectance of the MSI under the CCD3 angle and then convolve it with the relative spectral responses (RSRs) of CCD3 for spectral difference correction and judge whether this approach is more advantageous than SBAF. The investigation results will aid in analyzing the suitability and robustness of this cross-calibration method for the CCD3 sensor and facilitate monitoring the attenuation of its sensor signals during orbit, ensuring that the image data acquired by CCD3 can be effectively and broadly utilized across various fields.

This study is structured as follows: Section 2 introduces the CCD sensor, the MSI sensor, the MODIS sensor, the test sites, and the datasets. The construction process of the BRDF model using the random forest algorithm and the spectral interpolation convolution method used to correct the spectral difference between the two sensors are outlined in Section 3. Section 4 calculates the relative errors between the cross-calibration results presented in this study and the official calibration coefficients (OCCs), as well as the measured values from the Baotou sandy site. Section 5 analyzes the advantages of the method proposed in this study with respect to the light-matching cross-calibration and the radiative transfer cross-calibration, evaluates the influence of different BRDF models and different spectral correction methods on the calibration results, presents other influencing factors in the calibration process, and provides the total uncertainty. Section 6 summarizes the proposed method, presents the conclusions, and offers suggestions for future research.

2. Satellites, Test Sites, and Datasets

2.1. Satellites

The HuanJing-2A (HJ-2A) satellite was successfully launched by a Long March 4B launch vehicle on 27 September 2020, with a 16 m payload consisting of four CCD cameras and a 5-year design lifetime [25]. A single CCD camera has a coverage width of more than 200 km, and four splices can achieve a total width of more than 800 km, with a revisit cycle of 4 days. The data acquisition capability, technical performance, and accuracy of remote sensing data have been greatly improved compared with those of the HJ-1A/B satellite [26]. In addition to the commonly used blue, green, red, and near-infrared (NIR) bands, a “red edge” band, which effectively captures the unique spectral characteristics of crops, has also been added, and it is of great significance to research on remote sensing [27]. Additionally, the CRESDA can freely download HJ-2A satellite images.

Sentinel-2 is an Earth observation mission under the Copernicus program of the European Space Agency (ESA), divided into two satellites, 2A and 2B [28]. It is equipped with MSI that covers 13 bands, has a swath width of up to 290 km, and orbits at an altitude of 786 km, providing a revisit period of 10 days for one satellite and 5 days when both satellites are operational. It can detect wavelengths from visible and NIR to short-wave infrared (SWIR), with different resolutions of 10 m, 20 m, and 60 m and calibrations with up to about 3% accuracy [29]. Level 1C products can be downloaded freely from the ESA.

MODIS, installed on the Terra satellite, was successfully launched on 18 December 1999. It has 36 spectral bands with a spectral range from 0.4 μm to 14.4 μm [22]. Currently, MODIS data products are widely used, and their accuracy has been tested [30,31]. According to the research needs of this study, the MOD02HKM product, which provides apparent reflectance, the MOD09GA product, which provides surface reflectance, the MOD03 product, which provides solar/viewing angle information, and the MOD04_L2 product, which provides aerosol optical depth value (AOD), are downloaded [19].

In this study, the blue, green, red, NIR, and red edge, corresponding to the bands of CCD3 and the MSI, are selected for the research on cross-calibration. Table 1 lists the

wavelength range, spatial resolution, swath width, and revisit cycle of the corresponding bands of the CCD3 and MSI sensors, and Figure 1 demonstrates the RSRs of the two sensors in the five bands.

Table 1. Information on the corresponding bands of CCD3 and MSI.

Sensor	Band Name	Wavelength Range (nm)	Spatial Resolution (m)	Swath Width (km)	Revisit Cycle (d)
CCD3	Blue	450–520	16	200	4
	Green	520–590			
	Red	630–690			
	NIR	770–890			
	Red edge	690–730			
MSI	Blue	460–520	10	290	5
	Green	540–580			
	Red	650–680			
	NIR	790–900	20		
	Red edge	690–730			

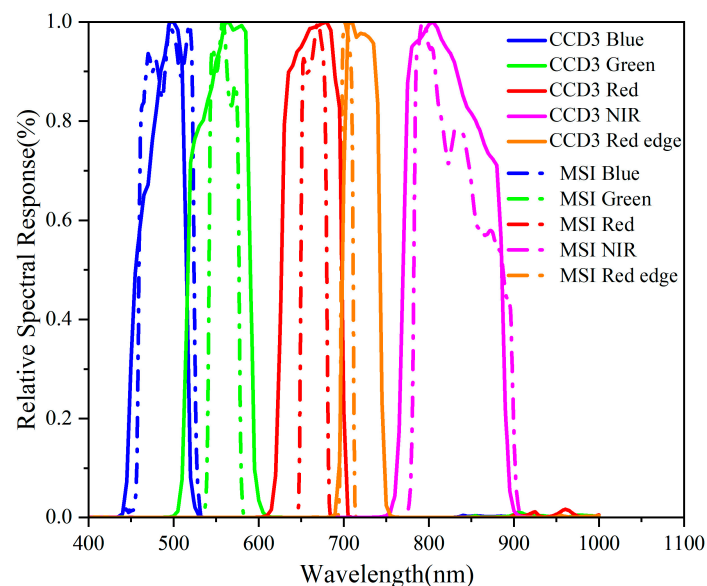


Figure 1. RSRs of CCD3 and MSI.

2.2. Test Sites

The Dunhuang radiometric calibration site (DRCS) is a radiation calibration site in China, situated in the Dunhuang area of Jiuquan City, Gansu Province. The whole site spans approximately 30 km by 30 km, located between the geographic coordinates of 40.04°N to 40.28°N and 94.17°E to 94.50°E (as illustrated in Figure 2), with an elevation of around 1200 m above sea level [32,33]. As a national radiation calibration field, it has been internationally recognized by the virtue of its uniform and flat ground surface, wide range, low precipitation, small atmospheric fluctuations, etc., and is often used to carry out research on site calibration experiments [34]. It is also a radiation transmission platform for evaluating the difference in radiation between two kinds of sensors [35]. Therefore, the DRCS is used as a calibration site in this study.

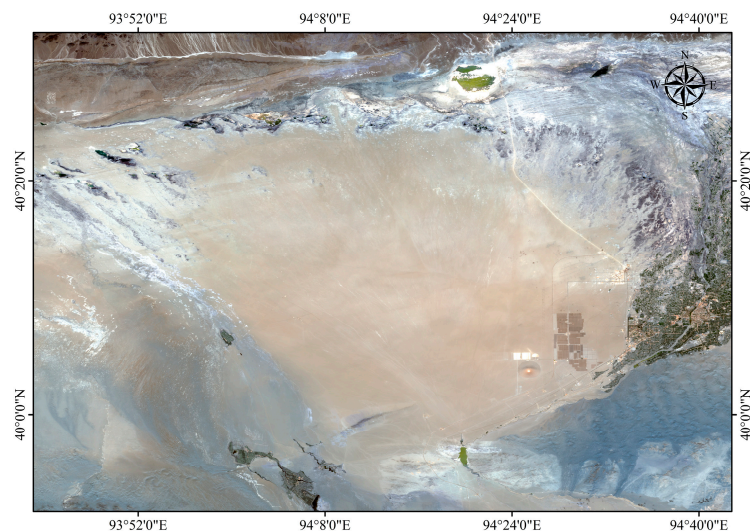


Figure 2. DRCS from CCD3 image on 9 May 2022.

The Baotou sandy site located in the city of Bayannur, Inner Mongolia, is a remote sensing field calibration site often referred to as the “Baotou Site”, situated at the geographic coordinates 40.87°N , 109.62°E (as illustrated in Figure 3), with an altitude of approximately 1270 m above sea level. The site is flat and open, dry with little rain, and one of the first demonstration sites for the Radiometric Calibration Network (RadCalNet) [36]. Reflectance measurements of both TOA and BOA in the 400–1000 nm spectral range are taken at 10 nm intervals every 30 min, accompanied by a series of automated spectral and atmospheric parameter measurements [37,38]. Therefore, the Baotou sandy site is used as a validation site in this study.



Figure 3. Baotou sandy site from MSI image on 2 March 2022.

2.3. Datasets

For this study, CCD3 and MSI images that passed over the DRCS on the same day in 2022 are selected. The transit time difference between the images is less than 1 h, suggesting that the atmospheric and surface conditions remained relatively stable during this period. Cloud cover must be absent over the DRCS, as clouds can interfere with the spatial and spectral characteristics of the site [39]. Furthermore, the coefficient of variation (CV) is

less than 3%, which has been widely used to ensure radiometric spatial homogeneity at calibration sites, and the formula is shown below [34,40]:

$$CV = \frac{\sigma}{\mu} \times 100\% \quad (1)$$

In this equation, σ represents the standard deviations (SDs) within the pixel windows. μ represents the mean within the pixel windows. Through data search, a total of five valid calibrated image pairs from 2022 are collected, and the image information for both sensors on the calibration days is shown in Table 2.

Table 2. Valid image pair information for DRCS and Baotou sandy site in 2022. VZ, SZ, VAZ, and SAZ denote the viewing zenith angle, solar zenith angle, view azimuth angle, and solar azimuth angle, respectively.

Site	Data	Sensors	Time	VZ (°)	SZ (°)	VAZ (°)	SAZ (°)
DRCS	8 February 2022	CCD3	13:05	8.4215	56.6671	103.4571	164.8759
		MSI	12:47	8.5310	57.5814	279.3340	159.9170
	6 April 2022	CCD3	12:57	8.4153	35.6701	103.6651	158.9273
		MSI	12:37	8.3255	37.0937	97.1749	151.1280
	1 May 2022	CCD3	13:07	8.4139	26.3112	103.5479	161.6297
		MSI	12:37	8.3934	28.6676	97.9633	146.9239
	9 May 2022	CCD3	13:02	8.4189	24.4026	103.5665	157.8442
		MSI	12:47	8.4819	25.5119	279.2809	150.0180
	23 June 2022	CCD3	13:01	8.4165	19.2089	103.5895	147.7677
		MSI	12:47	8.6379	20.7595	278.6671	139.7400
Baotou sandy site	12 April 2022	CCD3	12:05	8.9038	33.4352	103.4926	161.2189
	1 October 2022	CCD3	12:03	8.9019	44.3239	103.4880	170.2459

Given that the spatial resolutions of CCD3 and the MSI are different and resampling affects the original radiometric information of the image and the accuracy of the cross-calibration [8], this study focuses on the center of the DRCS (approximately 80 m × 80 m) as the research target. For the MSI sensor, 8 × 8 pixel windows are selected from 10 m resolution images, 4 × 4 pixel windows from 20 m resolution images, and 5 × 5 pixel windows from 16 m resolution images with the corresponding CCD3 sensor [17,21].

The CCD3 images passing over the Baotou sandy site in 2022 are also selected, ensuring no cloud cover obscures the experimental area. As CCD3 transits the Baotou sandy site around 12:05 (local standard time), the TOA reflectance data from the file (*.output) downloaded from the RadCalNet portal (<https://www.radcalnet.org>, accessed on 3 February 2024) should be valid at 12:00 (local standard time) [23]. With data retrieval, a total of two valid images from 2022 are collected as validation data from the Baotou sandy site, and the image information is shown in Table 2.

As there is an angle difference between the two sensors, BRDF correction needs to be considered. This is why a total of 70 MODIS images in 2022 transiting the DRCS are collected to extract angle and reflectance information, and no cloud occlusion is allowed. The extracted reflectance values should have a CV of less than 3% to ensure feature homogeneity, while outliers are rejected with the condition of mean ± two times the SDs [17,41]. The solar/viewing geometry information is extracted from the MOD03 product, and the geometry information is shown in Figure 4.

Additionally, because the CCD3 sensor provides only viewing geometry information at the center point, the target research area may not be located at the image's centroid position. Since the geometry influences the calibration results, this study applies the angle correction method proposed by Long et al. [42] to adjust the CCD3 viewing angle. The geometry information at the center point of the DRCS for the MSI is extracted from the file (*.hdr) after reprojecting.

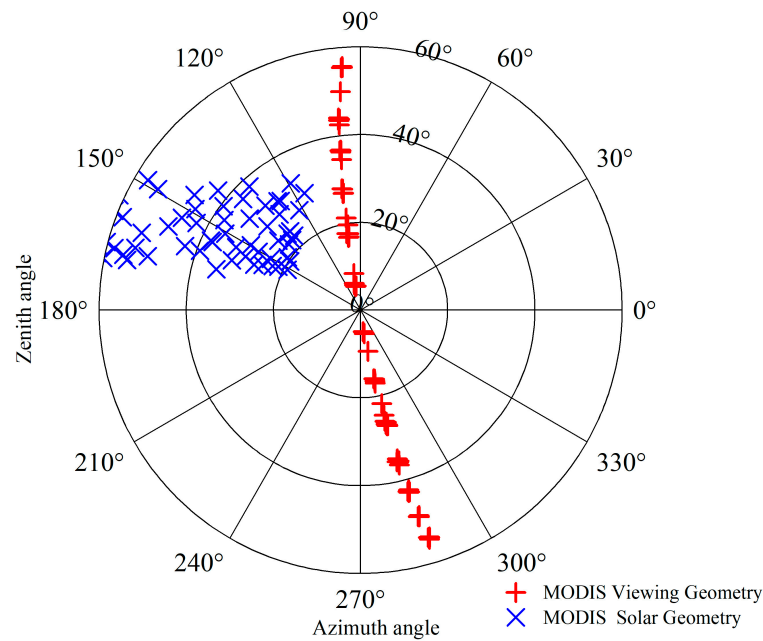


Figure 4. The geometry information of time-series MODIS images in 2022.

3. Methodology

In this study, the random forest algorithm and a spectral interpolation convolution method are proposed for the cross-calibration of HJ-2A/CCD3 using Sentinel-2/MSI with high radiometric performance as a reference sensor. A flowchart of this method is shown in Figure 5.

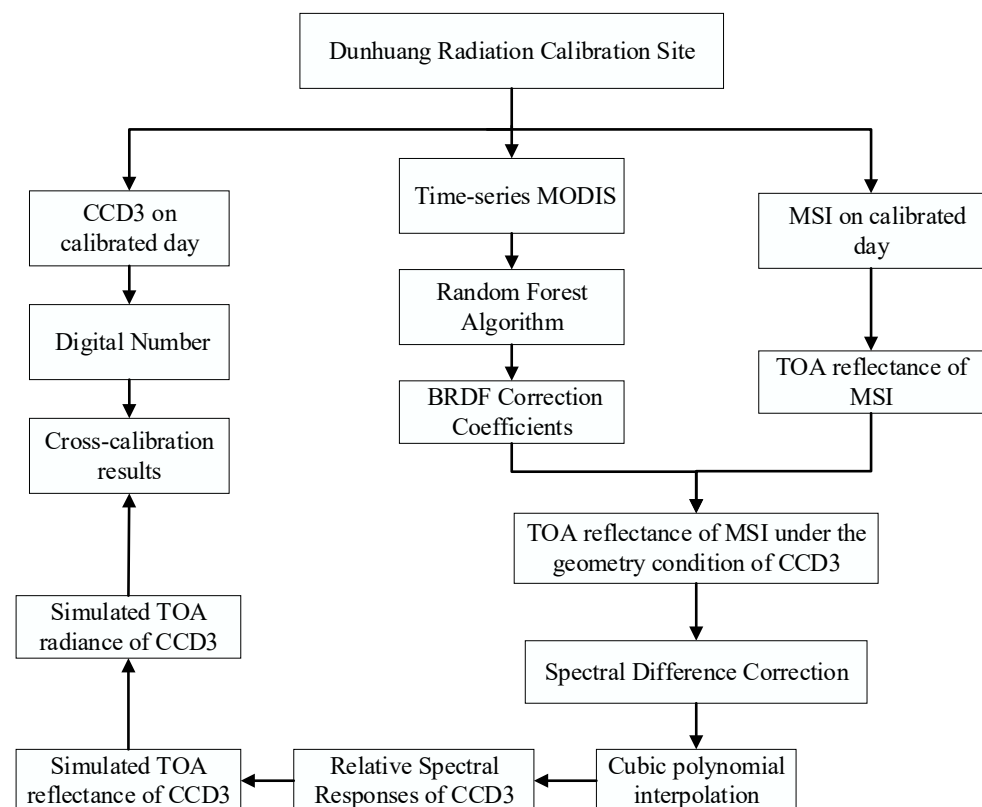


Figure 5. Flowchart of the experiment.

The cross-calibration method for HJ-2A/CCD3 based on Sentinel-2/MSI includes the following seven steps.

1. Utilizing the time-series MODIS imagery in 2022, the solar zenith angle, solar azimuth angle, view zenith angle, view azimuth angle, and TOA reflectance at the center point of the DRCS are extracted to calculate the volumetric scattering kernel, K_{vol} , and geometric optical scattering kernel, K_{geo} , in order to construct the stable target dataset required by the model [43,44].

$$K_{vol}(\theta, \varphi, \phi) = \frac{(\pi/2 - \zeta) \cos \zeta + \sin \zeta}{\cos \theta + \cos \varphi} - \frac{\pi}{4} \quad (2)$$

$$K_{geo}(\theta, \varphi, \phi) = \frac{1}{\pi} (t - \sin t \cos t) (\sec \theta + \sec \varphi) - \sec \theta - \sec \varphi + \frac{1}{2} (1 + \cos \zeta) \sec \theta \sec \varphi \quad (3)$$

In this equation, θ is the viewing zenith angle, φ is the solar zenith angle, ϕ is the relative azimuth angle, and t is calculated from these three angles [45]. ζ is the scattering angle [17].

2. The K_{vol} and K_{geo} are put into the random forest algorithm, where 70% are randomly selected as the training set and 30% as the validation set to construct the BRDF model. To evaluate the BRDF model's accuracy, the validation set is used to calculate the root-mean-square errors (RMSEs) (by Equation (4)) between the simulated and the measured TOA reflectance of the MODIS image [5], and the results are displayed in Table 3. It can be seen for the constructed BRDF model using the random forest algorithm that all have RMSEs of less than 0.96%, which proves that the model for the DRCS has high precision in 2022 [21].

Table 3. RMSEs between the simulated and measured TOA reflectance of the random forest algorithm for DRCS in 2022.

Blue	Green	Red	NIR
0.96%	0.73%	0.69%	0.74%

$$\text{RMSE} = \sqrt{\frac{\sum_1^N (\rho^{rf} - \rho^{ref})^2}{N}} \quad (4)$$

In this equation, ρ^{rf} and ρ^{ref} denote the simulated reflectance obtained by the random forest algorithm and the measured TOA reflectance obtained from the MODIS; and N is the number of images used to construct the validation set.

3. The BRDF correction coefficients, C , are derived from $\rho^{\text{CCD3_simulate}}$ and $\rho^{\text{MSI_simulate}}$, which are counted by the solar/viewing geometry angle information, as well as the random forest algorithm [43]. Since the MODIS sensor has no red edge band, the BRDF correction coefficient in the red edge band of CCD3 is set to 1.0 in this study [15].

$$C = \frac{\rho^{\text{CCD3_simulate}}}{\rho^{\text{MSI_simulate}}} \quad (5)$$

4. The TOA reflectance of the MSI image on the day of calibration, ρ^{MSI} , in the five bands is converted to that under the viewing angles of CCD3, $\rho^{\text{CCD3_MSI}}$, by [15,46] the following:

$$\rho^{\text{CCD3_MSI}} = C \times \rho^{\text{MSI}} \quad (6)$$

5. The spectral difference between the two sensors is corrected using the cubic polynomial interpolation to interpolate $\rho^{\text{CCD3_MSI}}$ into a continuous spectrum curve,

$\rho^{\text{CZ_CCD3_MSI}}$, then convolving with the RSRs of the CCD3 and using it as the TOA reflectance at the CCD3 [23].

$$\rho^{\text{CCD3}} = \frac{\int \rho^{\text{CZ_CCD3_MSI}} \times \text{RSR}_{\text{CCD3}}(\lambda) d\lambda}{\int \text{RSR}_{\text{CCD3}}(\lambda) d\lambda} \quad (7)$$

In the formula, RSR_{CCD3} is the RSRs of CCD3.

6. According to Equation (7), the TOA radiance at the pupil of CCD3, L^{CCD3} , can be calculated as follows [19]:

$$L^{\text{CCD3}} = \frac{\rho^{\text{CCD3}} \times \text{ESUN} \times \cos \theta}{\pi d^2} \quad (8)$$

where ESUN is the TOA solar irradiance, calculated from the convolution of the WRC solar spectrum curve [10], θ is the solar zenith angle for the CCD3 sensor, and d is the Sun–Earth distance.

7. Finally, Gain is the desired calibration coefficient for CCD3 [39,46].

$$\text{Gain} = \frac{L^{\text{CCD3}}}{\text{DN}^{\text{CCD3}}} \quad (9)$$

where DN^{CCD3} is the average digital number (DN) of the 5×5 -pixels windows of CCD3.

4. Results

4.1. Cross-Calibration Coefficients

Through the above method, the cross-calibration coefficients and SDs of the five calibration day images in 2022 are derived. Table 4 shows that the SDs for the five bands are less than 0.23%, indicating that the calibration coefficients across different dates exhibit good consistency [15]. This demonstrates that the cross-calibration method proposed in this study is stable.

Table 4. Cross-calibration coefficients and the SDs, FCCs, and OCCs of CCD3 in 2022.

Band	8 February 2022	6 April 2022	1 May 2022	9 May 2022	23 June 2022	SDs	FCCs	OCCs
Blue	0.0663	0.0673	0.0666	0.0631	0.0623	0.0023	0.0647	0.0657
Green	0.0544	0.0549	0.0539	0.0519	0.0516	0.0015	0.0530	0.0526
Red	0.0497	0.0508	0.0496	0.0480	0.0476	0.0013	0.0489	0.0473
NIR	0.0560	0.0576	0.0561	0.0554	0.0548	0.0010	0.0559	0.0555
Red edge	0.0534	0.0559	0.0546	0.0548	0.0548	0.0009	0.0549	0.0534

Additionally, the cross-calibration coefficients of the five images are linearly fitted for the purpose of subsequent tests, ultimately obtaining the total cross-calibration coefficients in 2022. The fitted cross-calibration coefficients (FCCs) are presented in Table 4 and Figure 6.

4.2. Validation of Cross-Calibration Coefficients with the OCCs

The cross-calibration coefficients are compared with the CCD3 sensor site calibration coefficient published by CRESDA in 2022 to calculate the relative error, which is defined as the absolute value of “cross-calibration coefficients/OCCs–1” [15,41]; then, average relative errors on the different calibration days are calculated, and the FCCs and OCCs are also used to count the relative error. The error results are shown in Table 5.

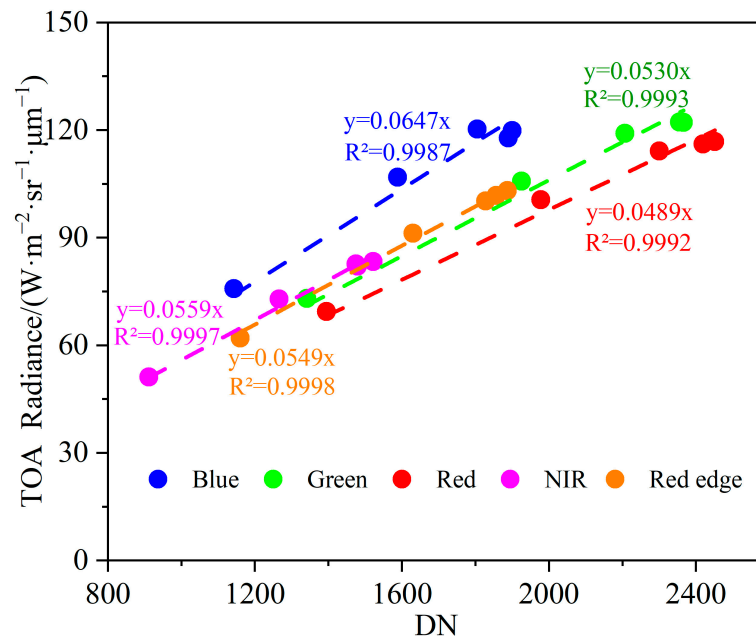


Figure 6. Fitting of cross-calibration coefficients for each band of the CCD3.

Table 5. Relative errors between cross-calibration coefficients and OCCs at DRCS.

Band	8 February 2022	6 April 2022	1 May 2022	9 May 2022	23 June 2022	Average	FCCs
Blue	0.85%	2.40%	1.41%	4.03%	5.12%	2.76%	1.48%
Green	3.51%	4.42%	2.56%	1.32%	1.88%	2.74%	0.80%
Red	5.51%	7.49%	4.86%	1.49%	0.68%	3.93%	3.38%
NIR	0.98%	3.71%	1.00%	0.09%	1.31%	1.42%	0.63%
Red edge	0.07%	4.73%	2.31%	2.70%	2.59%	2.48%	2.72%

The results show that the relative errors of all bands to the OCCs are less than 7.49%, the average relative errors are less than 3.93%, and the relative errors of the FCCs are less than 3.38%, which suggests that the method proposed in this study is applicable to the CCD3 sensor.

4.3. Validation of Cross-Calibration Results with the Baotou Sandy Site

In this study, the measured TOA reflectance (*.output) of the Baotou sandy site is first interpolated to 1 nm intervals and then convolved with the RSRs of CCD3, eventually taking the interpolated and convolved reflectances (ICRs) as the true value. Subsequently, the FCCs along with the OCCs are converted to reflectance and then compared to ICRs to determine the relative errors of the two validation images. Relative error is defined as the absolute value of “reflectance calculated based on FCCs/ICRs – 1” and the absolute value of “reflectance calculated based on OCCs/ICRs – 1”, respectively [19,21]. Then, the average relative error of the two validation images is also calculated, and the results are shown in Figure 7.

As can be seen from Figure 7, the maximum average relative error between the OCCs and ICRs is 4.44% and 4.11% between the FCCs and ICRs. Moreover, except for the NIR band, which has a larger error, the average relative errors calculated for all bands are better than those of the OCCs. This indicates that the method used in this study is suitable for research on CCD3.

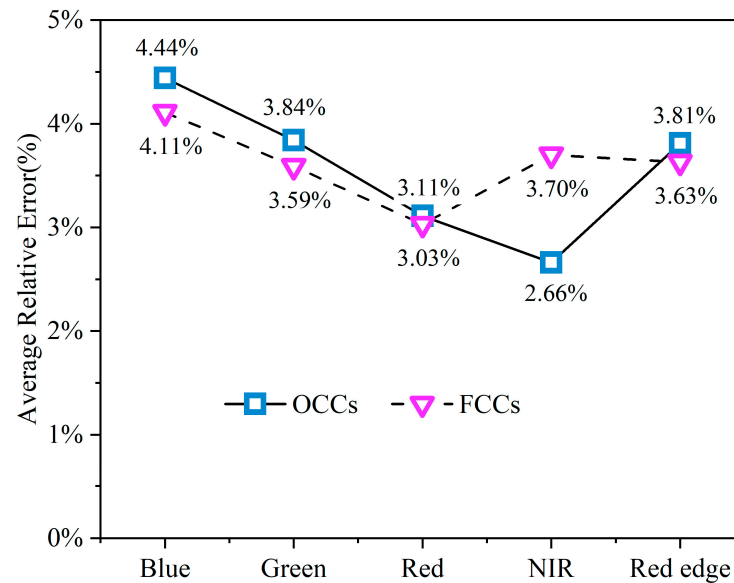


Figure 7. Average relative error of the ICRs with reflectance calculated based on OCCs and FCCs.

5. Discussion

In order to analyze the suitability and stability of this proposed cross-calibration method for the CCD3 sensor, we will discuss the calibration results according to the following schemes:

5.1. Cross-Calibration Results Based on the Light-Matching Method

The light-matching method achieves cross-calibration by comparing images acquired by different sensors at the same time, at the same location, and at the same observation angle [47]. Therefore, the calibration coefficient of the sensor to be calibrated needs to be obtained using a linear regression analysis [48] between the radiance at the pupil of the reference satellite sensor (i.e., also the radiance at the pupil of the satellite to be calibrated) and the DN value of the satellite image to be calibrated [12,49]. In this section, the light-matching method is used to obtain the cross-calibration coefficients for the five bands of the CCD3, which has a similar band setup to the MSI, using the MSI sensor as a reference, as shown in scheme (a) in Table 6.

Table 6. The research schemes to be conducted.

Schemes	BRDF	Spectral Difference
(a)	Non-consideration	Non-consideration
(b)	Ross–Li (MODIS)	SBAF
(c)	Ross–Li (MODIS)	Interpolation convolution
(d)	Random forest algorithm (MODIS)	SBAF
(e)	Random forest algorithm (MSI)	Interpolation convolution

Parentheses indicate the data sources used to construct the BRDF.

From Table 7, it can be seen that the results calculated based on the light-matching method differ significantly from the OCCs and from Figure 8; its maximum relative error with respect to ICRs is 11.41%. This illustrates the fact that even if the difference in the angles of these two sensors is not significant, the light-matching method may lead to a large error because it cannot take into account the spectral differences between the sensors.

Table 7. Relative errors between cross-calibration results based on the light-matching method and OCCs.

Band	8 February 2022	6 April 2022	1 May 2022	9 May 2022	23 June 2022	FCCs
Blue	12.07%	1.37%	0.75%	0.09%	3.79%	1.14%
Green	12.36%	2.47%	1.60%	1.44%	4.89%	2.40%
Red	10.44%	4.55%	3.15%	1.81%	7.99%	4.82%
NIR	15.75%	0.63%	2.11%	3.60%	3.35%	2.70%
Red edge	6.82%	9.51%	7.21%	14.63%	19.59%	11.16%

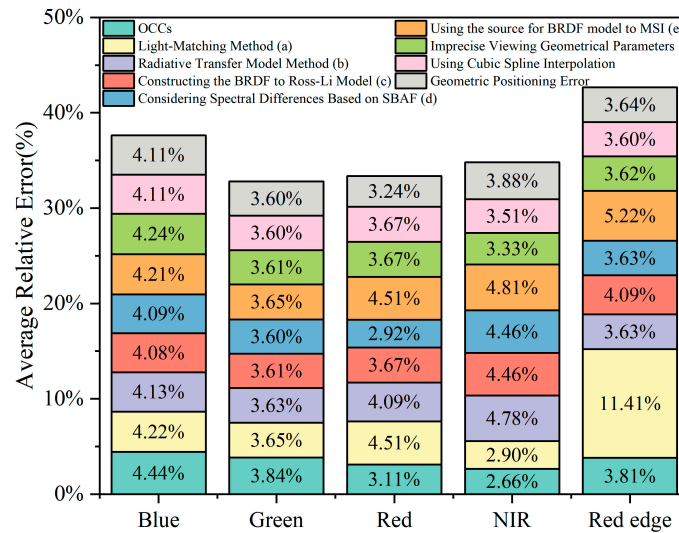


Figure 8. Average relative error of ICRs with reflectance calculated by OCCs and other cross-calibration coefficients after fitting.

5.2. Cross-Calibration Results Based on the Radiative Transfer Model Method

The radiative transfer model method takes into account the effects of viewing geometry and spectral differences of sensors on the calibration results [47,49]. The approach differs from the one proposed in this study mainly in the different methods used to consider the differences between the two sensors, as described in scheme (b) of Table 6. The BRDF parameters are firstly derived by the Ross–Li BRDF model with time-series MODIS images [15], and they are shown in Table 8. Then, using the MSI solar/viewing geometry and the CCD3 solar/changed-viewing geometry on the day of the calibration to calculate the BRDF correction coefficients [17], the TOA reflectance for the MSI image is converted to the viewing angles as the CCD3 by Equation (6). After, the MOD09GA surface reflectances are then extracted, and cubic polynomial interpolation is applied to acquire continuous spectral curves (see Figure 9), which are subsequently convolved with the RSRs of CCD3 and the MSI to derive the equivalent surface reflectance for each band [39]. Next, the 6S radiative transfer model, in which the input solar/viewing angle information is obtained from CCD3 and the AOD values are obtained from MOD04_L2, is used to convert the equivalent surface reflectance to the TOA reflectance to evaluate the SBAF parameters (as shown in Table 9) [19]. Finally, the simulated TOA radiance for CCD3 is determined by combining the SBAF parameters and the BRDF correction coefficients to obtain the cross-calibration results [21].

Table 8. Ross–Li BRDF parameters of DRCS with MODIS in 2022.

BRDF Parameters	Blue	Green	Red	NIR
f_{iso}	0.2092	0.2473	0.2741	0.2967
f_{vol}	0.2264	0.1171	0.0954	0.1071
f_{geo}	−0.0110	0.0174	0.0236	0.0209

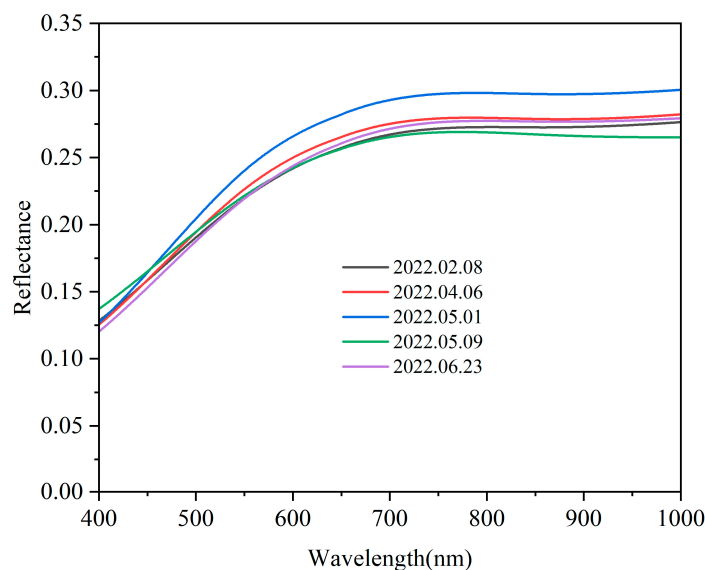


Figure 9. Continuous spectral curves after cubic polynomial interpolation for MOD09GA on calibration days.

Table 9. SBAF parameters between CCD3 and MSI.

Band	8 February 2022	6 April 2022	1 May 2022	9 May 2022	23 June 2022
Blue	0.9963	0.9926	0.9911	0.9950	0.9934
Green	1.0023	0.9970	0.9975	0.9987	0.9987
Red	0.9909	0.9910	0.9908	0.9915	0.9909
NIR	0.9548	0.9110	0.9140	0.9154	0.9156
Red edge	1.0061	1.0033	1.0042	1.0030	1.0048

The relative errors between the cross-calibration coefficients when using the radiative transfer model and the OCCs are given in Table 10. The maximum value of the relative error of the calibration coefficients is reduced from 9.08% based on the radiative transfer model to 7.49% based on the proposed method, and compared to FCCs, it is decreased from 7.30% to 3.38%. Concurrently, as shown in Figure 8, the average relative error of the cross-calibration results based on the radiative transfer model with ICRs is 4.78% at maximum, while the method proposed is only 4.11% at maximum. This indicates that the proposed random forest algorithm and spectral interpolation method present greater benefits compared to the radiative transfer model and can be used when considering the viewing and spectral difference between two sensors, which will consider the nonlinear relationships between kernels and reduce uncertainties due to the radiative transfer model, thus also obtaining stable results in all bands.

Table 10. Relative errors between cross-calibration results using the radiative transfer model and the OCCs.

Band	8 February 2022	6 April 2022	1 May 2022	9 May 2022	23 June 2022	FCCs
Blue	0.03%	1.42%	0.23%	4.12%	5.06%	2.01%
Green	3.51%	4.30%	2.47%	1.20%	1.66%	0.86%
Red	4.80%	7.00%	4.45%	1.65%	0.65%	3.21%
NIR	3.05%	5.59%	7.64%	7.95%	9.08%	7.30%
Red edge	0.12%	4.65%	2.39%	3.01%	2.91%	2.87%

5.3. Influences of Different Methods to Construct BRDF on Cross-Calibration Results

When constructing the BRDF model in step 2 of Section 3, the proposed method of the BRDF is the random forest algorithm. As different methods can affect the calibration

results, this summary recalculates the calibration coefficients by changing the method for constructing the BRDF model to Ross–Li [15], with the proposed spectral interpolation still used when considering spectral differences, as shown in scheme (c) from Table 6.

Table 11 illustrates the relative errors of the calibration coefficients using the Ross–Li BRDF model with OCCs, which shows that the relative errors are all less than 7.71%, and the fitted ones are all less than 4.36%, whereas the ones computed by the proposed method are all less than 7.49% and 3.38%, respectively. As can be seen from Figure 8, the average relative error of the Ross–Li BRDF model with ICRs has a maximum of 4.46% in scheme (c). These results show that using different methods to construct the BRDF model does impact the calibration results. However, in comparison, the calibration results obtained from the BRDF model constructed using the random forest algorithm are better for the cross-calibration of CCD3 than using the Ross–Li BRDF model and fully address the nonlinear relationships between kernel models.

Table 11. Relative errors between cross-calibration results using the Ross–Li BRDF model and OCCs.

Band	8 February 2022	6 April 2022	1 May 2022	9 May 2022	23 June 2022	FCCs
Blue	2.39%	2.02%	0.86%	2.60%	6.88%	1.00%
Green	3.11%	4.66%	2.53%	0.09%	2.33%	1.52%
Red	5.04%	7.71%	4.98%	2.80%	1.36%	4.36%
NIR	0.45%	3.76%	1.05%	0.28%	2.09%	0.56%
Red edge	0.10%	4.69%	2.30%	2.40%	2.40%	2.79%

5.4. Influence of Considering Spectral Differences Based on SBAF on Cross-Calibration Results

When considering the spectral difference in step 5 of Section 3, the method proposed in this study is a spectral interpolation convolution. In this part, utilizing the SBAF to correct the spectral difference and calculating the calibration coefficients with the BRDF method is still constructed using the random forest algorithm, as depicted in scheme (d) of Table 6.

The relative errors between the cross-calibration coefficients, for which the correction of spectral difference is SBAF, and the OCCs are calculated in Table 12. We obtained a maximum value of 8.24% based on the SBAF cross-calibration results with OCCs and a maximum value of 6.52% after fitting, while the maximum average relative error with the ICRs is 4.46%. This shows that the proposed spectral interpolation method is more advantageous than SBAF, thus also reducing the errors caused by the relatively large number of parameters involved in the radiative transfer model and improving the calibration accuracy.

Table 12. Relative errors between cross-calibration results using SBAF to consider spectral difference and the OCCs.

Band	8 February 2022	6 April 2022	1 May 2022	9 May 2022	23 June 2022	FCCs
Blue	1.64%	1.33%	0.25%	0.27%	0.73%	0.26%
Green	4.53%	4.29%	3.43%	0.61%	2.12%	2.60%
Red	6.44%	6.74%	4.36%	2.69%	3.87%	4.40%
NIR	4.22%	5.76%	7.64%	6.66%	6.71%	6.52%
Red edge	3.76%	4.58%	2.37%	7.02%	8.24%	5.24%

5.5. Influence of Different Data Sources for BRDF Models on Cross-Calibration Results

In step 1 of Section 3, the data source for the constructed BRDF model by using the random forest algorithm is MODIS. Whether it is suitable for constructing the BRDF model should be discussed. Therefore, we calculate the new calibration coefficients by changing the source for the BRDF model to MSI in the part, just as in scheme (e). The TOA reflectance of cloud-free and homogeneous MSI images crossing the DRCS, along with solar and viewing geometry information, are extracted to construct the BRDF model based on MSI.

The extracted reflectance's CV should be less than 3%, excluding reflectance other than the mean ± 2 times the SDs [40]. Finally, a total of 43 MSI (1C) images in 2022 are collected, and the reflectance information of the screened images is shown in Figure 10. The BRDF correction coefficients are calculated by Equations (2)–(5) (see Table 13).

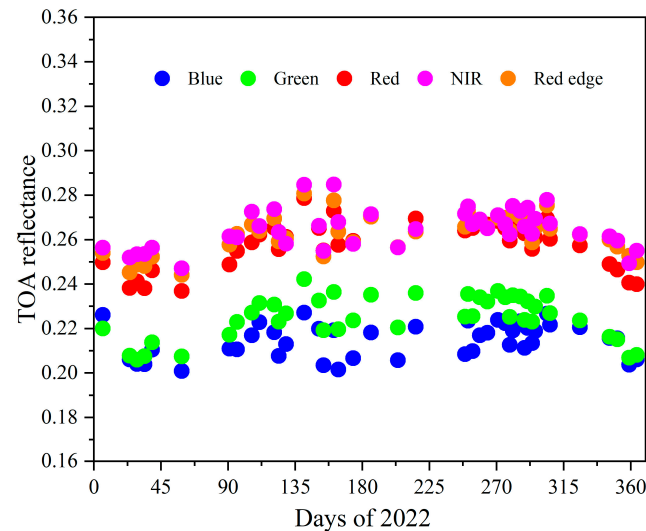


Figure 10. The reflectance information of time-series MSI images in 2022.

Table 13. BRDF correction coefficients of DRCS based on time-series MSI in 2022.

Band	8 February 2022	6 April 2022	1 May 2022	9 May 2022	23 June 2022
Blue	1.0067	1.0000	1.0002	1.0622	1.0750
Green	1.0506	0.9999	1.0094	1.0476	1.0642
Red	1.0478	0.9988	0.9989	1.0362	1.0475
NIR	1.0327	1.0001	0.9998	1.0524	1.0556
Red edge	1.0364	0.9993	0.9999	1.0389	1.0518

Table 14 shows the relative errors of the calibration coefficients using the MSI BRDF model by utilizing the random forest algorithm with OCCs, which demonstrates that the relative errors are all less than 5.06%. From Figure 8, the maximum relative error to ICRs is 5.22%. These results illustrate that the calibration results obtained from the BRDF model constructed using the MODIS, whose viewing angle does cover a wide range, are more reasonable for the cross-calibration of CCD3 than using MSI, whose viewing angle varies only in a small range.

Table 14. Relative errors between cross-calibration results using MSI to construct the BRDF model by utilizing the random forest algorithm and OCCs.

Band	8 February 2022	6 April 2022	1 May 2022	9 May 2022	23 June 2022	FCCs
Blue	0.98%	2.29%	1.07%	0.35%	1.19%	0.93%
Green	4.12%	4.39%	3.41%	0.61%	2.19%	2.55%
Red	6.90%	7.26%	4.84%	3.00%	4.44%	4.80%
NIR	0.58%	3.57%	1.01%	1.84%	1.28%	1.80%
Red edge	3.56%	4.70%	2.32%	6.83%	7.55%	5.06%

5.6. Influence of Imprecise Viewing Geometrical Parameters on Cross-Calibration Results

Because the viewing geometry affects the cross-calibration results to some extent, this study corrected the viewing geometry of CCD3 in step 3 of Section 3, in order to obtain precise geometrical parameters [42]. Therefore, in this section, how imprecise viewing geometrical parameters affect the calibration results will be discussed. That is, using the

viewing angle information of the image published in the file (*.xml), even if the center point of the DRCS is not positioned in the center of the images.

As shown in Table 15, the maximum relative error between the FCCs using imprecise viewing geometrical parameters and the OCCs is 4.04%, with an average relative error of 4.24% at maximum when compared to the ICRs. When the angles are changed using Long’s proposed method, the maximum relative error with OCCs is 3.38% from Table 5 and 4.11% with ICRs from Figure 8. This demonstrates that the viewing geometry affects the calibration results, and the calibration accuracy is improved to some extent after the correction of the viewing angle.

Table 15. Relative errors between cross-calibration results using imprecise viewing geometrical parameters and OCCs.

Band	8 February 2022	6 April 2022	1 May 2022	9 May 2022	23 June 2022	FCCs
Blue	1.14%	2.63%	1.19%	4.80%	5.43%	1.95%
Green	2.87%	5.28%	2.34%	1.04%	1.34%	1.06%
Red	6.41%	8.02%	4.65%	2.77%	1.37%	4.04%
NIR	0.25%	4.09%	0.80%	0.89%	1.79%	0.27%
Red edge	0.64%	5.27%	2.09%	2.45%	2.54%	2.62%

5.7. Influence of Different Interpolation Methods on Cross-Calibration Results

During the interpolation process in step 5 of Section 3, this study adopts the cubic polynomial interpolation method. Different interpolation methods will also have a certain impact on the calibration results; as such, this section will use cubic spline interpolation instead of cubic polynomial interpolation to explore its effect on the calibration results [15,17].

Table 16 shows the relative errors of the calibration coefficients using cubic spline interpolation and OCCs, these results are not much different from the results obtained using cubic polynomial interpolation, as shown in Table 5. Additionally, as can be seen in Figure 8, both methods exhibit the same maximum average relative error of 4.11%, in contrast with the ICRs, demonstrating that cubic polynomial interpolation and cubic spline interpolation are both suitable for obtaining the continuous spectral profile.

Table 16. Relative errors between cross-calibration results using the cubic spline interpolation method and OCCs.

Band	8 February 2022	6 April 2022	1 May 2022	9 May 2022	23 June 2022	FCCs
Blue	1.99%	2.66%	1.89%	2.48%	3.72%	0.47%
Green	3.58%	4.38%	2.56%	0.99%	1.62%	0.95%
Red	5.57%	7.51%	4.99%	2.54%	1.53%	3.61%
NIR	0.89%	3.86%	1.13%	0.42%	1.58%	0.52%
Red edge	0.50%	4.98%	2.42%	1.16%	1.30%	2.06%

5.8. Influence of Geometric Positioning Error on Cross-Calibration Results

Owing to the existence of offsets caused by varying image accuracies, two different sensors may locate different features, even at the same latitude and longitude. Therefore, this section will discuss the effect of the cross-calibration results when the sliding windows (5×5 pixels) of the CCD3 image are shifted by 1 pixel (approximately 16 m) [17].

From Table 17, the maximum relative error between the calibration results after correcting the geometric positioning error and OCCs is 7.65%. After fitting, the maximum relative error is 3.66%, and with the ICRs, it is 4.11%. The differences between the maximum relative error from Tables 5 and 17 are 0.16% and 0.28%, respectively. When using the Baotou sandy site, the maximum difference is the same. This explains the homogeneity of the experimental area, which is applicable to this study.

Table 17. Relative errors between calibration results after correcting the geometry positioning error and OCCs.

Band	8 February 2022	6 April 2022	1 May 2022	9 May 2022	23 June 2022	FCCs
Blue	1.02%	2.51%	1.57%	3.99%	4.99%	1.37%
Green	3.64%	4.54%	2.80%	1.21%	1.59%	0.99%
Red	5.41%	7.65%	5.24%	1.69%	0.99%	3.66%
NIR	1.29%	3.88%	1.30%	0.07%	0.94%	0.88%
Red edge	0.31%	4.96%	2.51%	2.87%	2.92%	2.94%

5.9. Total Uncertainty

In this section, the total uncertainty of the final cross-calibration coefficients is calculated, acknowledging that not all factors can be quantified. Six main influencing factors are considered in this study.

1. BRDF: During the construction of the BRDF model, there are several factors that can lead to variations in the calibration results, such as different BRDF models, TOA reflectance of MODIS, ignored BRDF correction coefficients in the red edge band, and the solar/viewing angles, so the uncertainty is taken into account. Firstly, by using the random forest algorithm and the Ross–Li model for constructing the BRDF model, the maximum differences between the cross-calibration coefficients are derived for each band, which is taken as the uncertainty of different BRDF models. Secondly, for the MODIS BRDF model constructed using the random forest algorithm, the calibration accuracy of MODIS is about 2% [10], which is treated as the uncertainty associated with the TOA reflectance of MODIS. Thirdly, since the red edge band is set to 1 when calculating the BRDF correction coefficients, its effect on the calibration uncertainty should be considered. The BRDF correction coefficients in the red edge band are increased by 0.01 and decreased by 0.01 to recalculate the relative errors between the new calibration coefficients and the OCCs. Then, the relative errors are then subtracted from each other, and the maximum difference obtained for the red edge is taken as the uncertainty. Fourthly, the errors of the solar angles are neglected [15]. In order to consider the errors of the viewing angles, we increased them by 0.1° and then used them to recalculate the new results. The maximum relative differences between the new cross-calibration coefficients and the coefficients given in Table 4 for each band are treated as the uncertainty values associated with the viewing angles [10]. Finally, these error values are calculated by the square root method as the uncertainty values with respect to BRDF, the results are shown in Table 18.
2. Reference satellite: Uncertainties due to the reference satellite need to be addressed. The calibration uncertainty of Sentinel-2/MSI is approximately 3% [35].
3. Viewing geometric parameter: The uncertainty caused by the viewing geometric parameter must be considered in the process of cross-calibration. The maximum difference in the relative error of the cross-calibration coefficients for five bands before and after the change in the CCD3 viewing angle is used as the value of the uncertainty related to the viewing geometric parameter, and the results are shown in Table 19.
4. Interpolation method: The interpolation method used can have an influence on the calibration results. The maximum value of the relative error between the calibration coefficients according to the cubic spline interpolation method and the calibration coefficients in Table 4 is calculated as the uncertainty value relevant to the interpolation method.
5. Geometric positioning error: Since geometric positioning errors also cause changes in the calibration results to some extent, the uncertainty caused by correcting for geometric positioning errors cannot be ignored. The results are shown in Table 19.
6. ESUN source: The ESUN values in this study are calculated by convolving the WRC solar spectrum curves with the RSRs of CCD3, whereas the solar irradiance of HJ-2A/CCD3 is not given in CRESDA. For this reason, the solar spectral curve

required for convolution shall not be negligible. The spectral curve is replaced from WRC to Kurucz, and the coefficients are recalculated, along with the maximum relative difference from Table 4. These values are used as the uncertainty associated with the ESUN source.

Table 18. Total uncertainty of BRDF.

Factors	Blue	Green	Red	NIR	Red Edge
Different BRDF models (%)	1.85	1.43	1.30	1.42	0.29
TOA reflectance of MODIS (%)	2.00	2.00	2.00	2.00	2.00
Ignored BRDF correction in red edge band (%)	0.00	0.00	0.00	0.00	2.10
Viewing angles (%)	1.92	0.56	1.55	1.10	0.00
Total uncertainty of BRDF (%)	3.33	2.52	2.84	2.69	2.91

Table 19. Total uncertainty of cross-calibration.

Symbol	Blue	Green	Red	NIR	Red Edge
BRDF (%)	3.33	2.52	2.84	2.69	2.91
Reference satellite (%)	3.00	3.00	3.00	3.00	3.00
Viewing geometric parameter (%)	1.97	0.83	1.26	0.79	0.72
Interpolation method (%)	1.61	0.34	1.04	0.33	1.50
Geometric positioning error (%)	0.17	0.30	0.36	0.37	0.33
ESUN source (%)	0.09	0.10	0.13	0.10	0.08
Total uncertainty (%)	5.16	4.03	4.46	4.14	4.51

The factors of the uncertainty and total uncertainty of the cross-calibration results are shown in Table 19. Overall, the total uncertainty calculated using the square root method is less than 5.16% [41].

6. Conclusions

In this study, in order to account for the nonlinear relationship between kernel models and the differences introduced by radiative transfer models, the random forest algorithm and a spectral interpolation convolution method are proposed, which are used to correct the viewing geometry difference and the spectral difference between two sensors, enabling the cross-calibration of the HJ-2A/CCD3 sensor with Sentinel-2/MSI as a reference satellite sensor. Valid time-series TOA reflectance images from the MODIS are collected in 2022 using the DRCS as the research area for the construction of the BRDF model. The viewing geometric difference between the two sensors is then corrected using the BRDF correction coefficients predicted by the random forest algorithm, followed by converting the TOA reflectance from the MSI to the CCD3 angle on the calibration date. Subsequently, the reflectance is first interpolated to obtain a continuous spectral profile, which is then convolved with the RSRs of CCD3 to obtain the simulated TOA reflectance. Finally, the cross-calibration coefficients for the CCD3 sensor are derived using the TOA radiance obtained from the simulation, along with the mean DN value extracted on the calibration day.

From the results of the cross-calibration method proposed in this study, it can be seen that the calibration coefficients of different dates do not differ much, and the SDs of various bands are less than 0.23%, demonstrating good consistency. Compared with the OCCs, the average relative errors are under 3.38%. When using the Baotou sandy site for testing, the FCCs have a maximum average relative error of 4.11% with ICRs, and the errors for the other bands are better compared to the OCCs, except for the NIR, which has a larger error.

As can be seen from the light-matching results, they have a large error with respect to the OCCs. It is shown that even if the angle difference between these two sensors is not significant, this may lead to unacceptable errors since it does not take into account the spectral differences between the channels. Then, the maximum value of the relative error of the calibration coefficients is reduced from 7.30% based on the radiative transfer model to 3.38% based on the proposed approach, and in contrast to ICRs, it is decreased from 4.78% to 4.11%.

These indicate that the proposed random forest algorithm and spectral interpolation method present a smaller error with OCCs and ICRs compared to the radiative transfer model, also taking full account of the nonlinear relationships between the kernels and reducing the error associated with the radiative transfer model. When the BRDF model is replaced with MSI, the calibration results have a relative error with the OCCs of 5.06% at maximum and 5.22% with ICRs, respectively. It is found that the calibration coefficients obtained using the MODIS sensor to construct the BRDF model, which has a large geometric coverage of viewing, are better than those obtained using MSI.

Simultaneously, the effects of the viewing geometrical parameters, different spectral interpolation methods, and geometric positioning errors on the results are discussed. It can be seen that the cubic spline and cubic polynomial interpolation methods, as well as the geometric positioning error, do not have much impact on the results. However, after correcting the viewing geometry parameters, the accuracy of the cross-calibration is improved to some extent. Meanwhile, uncertainties are considered, including the BRDF, difference reference, viewing geometric parameter, interpolation method, geometric positioning error, and ESUN sources. The total uncertainty of the cross-calibration results is less than 5.16%.

The applicability of the proposed method to the other three cameras of the HJ-2A will be examined in future work. Additionally, the potential issue of radiometric differences among different sensors on the same satellite will be considered. More RadCalNet sites will also be selected for calculating calibration coefficients to further evaluate the cross-radiometric calibration method for HJ-2A satellites and enhance the accuracy of on-orbit radiometric calibration for these cameras.

Author Contributions: Conceptualization, X.Z., Y.C. and J.H.; methodology, X.Z. and Y.C.; software, X.Z. and Y.C.; validation, Y.C.; formal analysis, X.Z.; investigation, Y.X.; resources, Y.X.; data curation, Y.C.; writing—original draft preparation, X.Z. and Y.C.; writing—review and editing, Y.X. and J.H.; visualization, J.H. and W.S.; supervision, Y.X., J.H. and W.S.; project administration, Y.X., J.H. and W.S.; funding acquisition, Y.X. and J.H. All authors have read and agreed to the published version of the manuscript.

Funding: This research was funded by the National Natural Science Foundation of China under Grants 42176176 and 42476169, the Science and Technology of Henan Province under Grant 242102320005, the Henan Province Higher Education Key Teachers Support Program under Grant 2024GGJS121, the Key Scientific Research Project Plan of University in Henan Province under Grant 24A420004, the Xuchang University Key Teachers Support Program under Grant XCXYQNGG2023014, the National Natural Science Foundation Cultivation Project of Xuchang University under Grants 2022GJPY007 and 2023GJPY019, and the Land Observation Satellite Supporting Platform of National Civil Space Infrastructure Project.

Data Availability Statement: The level 1A data for the HJ-2A/CCD3 sensor are available from the China Centre for Resources Satellite Data and Application (CRESDA, <https://data.cresda.cn/#/2dMap>, accessed on 3 February 2024). The level 1C products for Sentinel-2/MSI are available from the European Space Agency Copernicus Data Center (<https://dataspace.copernicus.eu/>, accessed on 3 February 2024). The MODIS data are available from the National Aeronautics and Space Administration (NASA, <https://ladsweb.modaps.eosdis.nasa.gov/>, accessed on 3 February 2024). The TOA measured reflectance data for the Baotou sandy sand are available from the Radiometric Calibration Network (RadCalNet, <https://www.radcalnet.org/#/>, accessed on 3 February 2024).

Acknowledgments: The author is grateful to CRESDA for supplying HJ-2A/CCD3 data, ESA for furnishing Sentinel-2/MSI data, and NASA for providing MODIS data. Appreciation is also extended to RadCalNet for delivering Baotou sandy site data. Additionally, the author thanks the anonymous reviewers for their valuable feedback.

Conflicts of Interest: The authors declare no conflicts of interest.

References

1. Li, G.; He, Y.; Hu, X.; Wang, J. Cross calibration technology for the same platform of FY-3 optical imager based on IR-MAD No-change pixels. *Natl. Remote Sens. Bull.* **2023**, *27*, 2337–2349. [[CrossRef](#)]

2. Lu, J.; He, T.; Liang, S.; Zhang, Y. An automatic radiometric cross-calibration method for wide-angle medium-resolution multispectral satellite sensor using Landsat data. *IEEE Trans. Geosci. Remote Sens.* **2022**, *60*, 5604011. [[CrossRef](#)]
3. Tang, H.; Tang, X.; Xie, J.; Chen, W.; Qian, Y. On-orbit radiometric calibration and validation of GF-7 satellite based on RadCalNet Baotou site. *Natl. Remote Sens. Bull.* **2023**, *27*, 1194–1204. [[CrossRef](#)]
4. Liu, K.; Ke, T.; Tao, P.; He, J.; Xi, K.; Yang, K. Robust radiometric normalization of multitemporal satellite images via block adjustment without master images. *IEEE J. Sel. Top. Appl. Earth Obs. Remote Sens.* **2020**, *13*, 6029–6043. [[CrossRef](#)]
5. Moghimi, A.; Sarmadian, A.; Mohammadzadeh, A.; Celik, T.; Amani, M.; Kusetogullari, H. Distortion robust relative radiometric normalization of multitemporal and multisensor remote sensing images using image features. *IEEE Trans. Geosci. Remote Sens.* **2022**, *60*, 5400820. [[CrossRef](#)]
6. Li, H.; Hao, S. A relative radiometric correction method for the scanning image of pushbroom satellite. *Optoelectron. Eng.* **2011**, *38*, 142–145.
7. Pesta, F.; Bhatta, S.; Helder, D.; Mishra, N. Radiometric non-uniformity characterization and correction of Landsat 8 OLI using earth imagery-based techniques. *Remote Sens.* **2014**, *7*, 430–446. [[CrossRef](#)]
8. Pahlevan, N.; Schott, J. Characterizing the relative calibration of Landsat-7 (ETM+) visible bands with Terra (MODIS) over clear waters: The implications for monitoring water resources. *Remote Sens. Environ.* **2012**, *125*, 167–180. [[CrossRef](#)]
9. Koukal, T.; Suppan, F.; Schneider, W. The impact of relative radiometric calibration on the accuracy of kNN-predictions of forest attributes. *Remote Sens. Environ.* **2007**, *110*, 431–437. [[CrossRef](#)]
10. Gao, H.; Gu, X.; Yu, T.; Sun, Y.; Liu, Q. Cross-calibration of GF-1 PMS sensor with Landsat 8 OLI and Terra MODIS. *IEEE Trans. Geosci. Remote Sens.* **2016**, *54*, 4847–4854. [[CrossRef](#)]
11. Chander, G.; Markham, B. Revised landsat-5 TM radiometric calibration procedures and postcalibration dynamic ranges. *IEEE Trans. Geosci. Remote Sens.* **2003**, *41*, 2674–2677. [[CrossRef](#)]
12. Ma, L.; Wang, N.; Gao, C.; Zhao, Y.; Yang, B.; Wang, X.; Han, Q.; Xu, N.; Song, P.; Liu, Y. On-orbit absolute radiometric calibration for optical remote sensing satellites: Progress and trends. *Natl. Remote Sens. Bull.* **2023**, *27*, 1061–1087. [[CrossRef](#)]
13. Fu, Q.; Min, X.; Li, X.; Sha, C.; Li, X.; Ma, G.; Pan, Z.; Guo, Y.; Li, Q.; Liu, G. In-flight absolute calibration of the CBERS-02 CCD sensor at the Dunhuang test site. *J. Remote Sens.* **2006**, *10*, 433–439.
14. Li, J.; Feng, L.; Pang, X. Comparison of the cross-calibration methods between image-based and RTM-BRDF for GF-1 images. *Acta Geod. Cartogr. Sin.* **2017**, *46*, 882–890.
15. Han, J.; Tao, Z.; Xie, Y.; Li, H.; Liu, Q.; Guan, X. A novel radiometric cross-calibration of GF-6/WFV with MODIS at the Dunhuang radiometric calibration site. *IEEE J. Sel. Top. Appl. Earth Obs. Remote Sens.* **2021**, *14*, 1645–1653. [[CrossRef](#)]
16. Wang, H.; He, Z.; Wang, S.; Zhang, Y.; Tang, H. Radiometric cross-calibration of GF-6/PMS and WFV sensors with Sentinel 2-MSI and Landsat 9-OLI2. *Remote Sens.* **2024**, *16*, 1949. [[CrossRef](#)]
17. Xie, Y.; Feng, D.; Shao, W.; Han, J.; Chen, Y. Radiometric cross calibration of HY-1C/COCTS based on Sentinel-3/OLCI. *IEEE J. Sel. Top. Appl. Earth Obs. Remote Sens.* **2024**, *17*, 10422–10431. [[CrossRef](#)]
18. Dong, J.; Chen, Y.; Chen, X.; Xu, Q. Radiometric cross-calibration of wide-field-of-view cameras based on Gaofen-1/6 satellite synergistic observations using Landsat-8 operational land imager images: A solution for off-nadir wide-field-of-view associated problems. *Remote Sens.* **2023**, *15*, 3851. [[CrossRef](#)]
19. Han, J.; Tao, Z.; Xie, Y.; Liu, Q.; Huang, Y. Radiometric cross-calibration of GF-4/PMS based on radiometric block adjustment. *IEEE Trans. Geosci. Remote Sens.* **2021**, *59*, 4522–4534. [[CrossRef](#)]
20. Niu, C.; Tan, K.; Wang, X.; Han, B.; Ge, S.; Du, P.; Wang, F. Radiometric cross-calibration of the ZY1-02D hyperspectral imager using the GF-5 AHSI imager. *IEEE Trans. Geosci. Remote Sens.* **2022**, *60*, 5519612. [[CrossRef](#)]
21. Han, J.; Tao, Z.; Xie, Y.; Li, H.; Guan, X.; Yi, H.; Shi, T.; Wang, G. Radiometric cross-calibration of GF-6/WFV sensor using MODIS images with different BRDF models. *IEEE Trans. Geosci. Remote Sens.* **2022**, *60*, 5409311. [[CrossRef](#)]
22. Liu, L.; Shi, T.; Gao, H.; Zhang, X.; Han, Q.; Hu, X. Long-term cross calibration of HJ-1A CCD1 and Terra MODIS reflective solar bands. *Sci. Rep.* **2021**, *11*, 7386. [[CrossRef](#)] [[PubMed](#)]
23. Han, J.; Tao, Z.; Xie, Y.; Li, H.; Yi, H.; Guan, X. Validation of the TOA products of the Baotou sandy site with Landsat8/OLI considering BRDF correction. *IEEE Trans. Geosci. Remote Sens.* **2023**, *61*, 5401611. [[CrossRef](#)]
24. Vermote, E.; Tanre, D.; Deuze, J.; Herman, M.; Morcette, J. Second simulation of the satellite signal in the solar spectrum, 6S: An overview. *IEEE Trans. Geosci. Remote Sens.* **1997**, *35*, 675–686. [[CrossRef](#)]
25. Bai, Z.; Dong, Y.; Zhu, J.; Sun, J.; Ma, L. System design and technology innovation of HJ-2A/B satellites. *Spacecr. Eng.* **2022**, *31*, 1–8.
26. Zhang, H.; Qin, W.; Wang, K.; Wang, Q.; Tao, P. On-orbit geometric calibration of the HJ-2A/B satellites' infrared sensors. *ISPRS Ann. Photogramm. Remote Sens. Spat. Inf. Sci.* **2024**, *X-1-2024*, 305–311. [[CrossRef](#)]
27. Li, Y.; Wu, J.; Zhong, B.; Shi, X.; Xu, K.; Ao, K.; Sun, B.; Ding, X.; Wang, X.; Liu, Q.; et al. Methods of sandy land detection in a sparse-vegetation scene based on the fusion of HJ-2A hyperspectral and GF-3 Sar data. *Remote Sens.* **2022**, *14*, 1203. [[CrossRef](#)]
28. Revel, C.; Lonjou, V.; Marcq, S.; Desjardins, C.; Fougny, B.; Coppolani-Delle Luche, C.; Guillemot, N.; Lacamp, A.-S.; Lourme, E.; Miquel, C.; et al. Sentinel-2A and 2B absolute calibration monitoring. *Eur. J. Remote Sens.* **2019**, *52*, 122–137. [[CrossRef](#)]
29. Li, S.; Ganguly, S.; Dungan, J.; Wang, W.; Nemani, R. Sentinel-2 MSI radiometric characterization and cross-calibration with Landsat-8 OLI. *Adv. Remote Sens.* **2017**, *6*, 147–159. [[CrossRef](#)]

30. Angal, A.; Xiong, X.; Shrestha, A. Cross-calibration of MODIS reflective solar bands with Sentinel 2A/2B MSI instruments. *IEEE Trans. Geosci. Remote Sens.* **2020**, *58*, 5000–5007. [[CrossRef](#)]
31. Xiong, X.; Kwo-Fu, C.; Wu, A.; Barnes, W.L.; Guenther, B.; Salomonson, V.V. Multiyear on-orbit calibration and performance of Terra Modis thermal emissive bands. *IEEE Trans. Geosci. Remote Sens.* **2008**, *46*, 1790–1803. [[CrossRef](#)]
32. Cui, Z.; Ma, C.; Zhang, H.; Hu, Y.; Yan, L.; Dou, C.; Li, X. Vicarious radiometric calibration of the multispectral imager onboard sdgsat-1 over the Dunhuang calibration site, China. *Remote Sens.* **2023**, *15*, 2578. [[CrossRef](#)]
33. Huang, D.; Li, X.; Zheng, X.; Wei, W.; Zhang, Q.; Guo, F. Evaluation and application of on-orbit calibration of the automated vicarious calibration system. *IEEE Trans. Geosci. Remote Sens.* **2023**, *61*, 1001115. [[CrossRef](#)]
34. Hu, X.; Wang, L.; Wang, J.; He, L.; Chen, L.; Xu, N.; Tao, B.; Zhang, L.; Zhang, P.; Lu, N. Preliminary selection and characterization of pseudo-invariant calibration sites in northwest China. *Remote Sens.* **2020**, *12*, 2517. [[CrossRef](#)]
35. Gao, C.; Liu, Y.; Qiu, S.; Li, C.; Ma, L.; Han, Q.; Liu, J.; Zhao, E.; Zhao, Y.; Qian, Y.; et al. Radiometric cross-calibration of GF-4/VNIR sensor with Landsat8/OLI, Sentinel-2/MSI, and Terra/MODIS for monitoring its degradation. *IEEE J. Sel. Top. Appl. Earth Obs. Remote Sens.* **2020**, *13*, 2337–2350. [[CrossRef](#)]
36. Liu, Y.; Ma, L.; Wang, R.; Zheng, Q.; Song, P.; Li, W.; Zhao, Y.; Wang, N.; Gao, C.; Hou, X.; et al. Time-series absolute radiometric calibration and trend analysis of the wide swath sensor onboard GF-6 satellite with automatic radiometric calibration site. *Natl. Remote Sens. Bull.* **2023**, *27*, 599–609. [[CrossRef](#)]
37. Tao, Z.; Han, J.; Xie, Y.; Li, H.; Yi, H.; Guan, X. A TOA spectral reflectance model of railroad valley playa site to compensate the missing Radcalnet data. *IEEE Trans. Geosci. Remote Sens.* **2024**, *62*, 5629110. [[CrossRef](#)]
38. Bouvet, M.; Thome, K.; Berthelot, B.; Bialek, A.; Czapla-Myers, J.; Fox, N.; Goryl, P.; Henry, P.; Ma, L.; Marcq, S.; et al. RadCalNet: A radiometric calibration network for earth observing imagers operating in the visible to shortwave infrared spectral range. *Remote Sens.* **2019**, *11*, 2401. [[CrossRef](#)]
39. Xie, Y.; Han, J.; Gu, X.; Liu, Q. On-orbit radiometric calibration for a space-borne multi-camera mosaic imaging sensor. *Remote Sens.* **2017**, *9*, 1248. [[CrossRef](#)]
40. Song, P.; Ma, L.; Zhao, Y.; Wang, N.; Li, W.; Han, Q.; Liu, Y.; Yao, W.; Zhang, B.; Ren, L.; et al. Construction and validation of the TOA reflectance reference model for stable land surface targets by using Golmud desert site as an example. *Natl. Remote Sens. Bull.* **2023**, *27*, 1099–1113. [[CrossRef](#)]
41. Guo, F.; Zheng, X.; Zhang, Y.; Wei, W.; Zhang, Z.; Zhang, Q.; Li, X. A wide-angle hyperspectral top-of-atmosphere reflectance model for the Libyan desert. *Remote Sens.* **2024**, *16*, 1406. [[CrossRef](#)]
42. Long, T.; Jiao, W.; He, G.; Wang, G.; Zhang, Z. Digital orthophoto map products and automated generation algorithms of Chinese optical satellites. *Natl. Remote Sens. Bull.* **2023**, *27*, 635–650. [[CrossRef](#)]
43. Liu, L.; Gao, H.; Pan, Z.; Qian, Y.; Han, Q.; Zhang, X.; Shi, T. Satellite-based time series calibration of GF1 WFV sensors for large view zenith angle observations. *Int. J. Remote Sens.* **2018**, *39*, 8293–8316. [[CrossRef](#)]
44. Lucht, W.; Schaaf, C.B.; Strahler, A.H. An algorithm for the retrieval of albedo from space using semiempirical BRDF models. *IEEE Trans. Geosci. Remote Sens.* **2000**, *38*, 977–998. [[CrossRef](#)]
45. Schaaf, C.; Gao, F.; Strahler, A.; Lucht, W.; Li, X.; Tsang, T.; Strugnell, N.C.; Zhang, X.; Jin, Y.; Muller, J.P.; et al. First operational BRDF, albedo nadir reflectance products from MODIS. *Remote Sens. Environ.* **2002**, *83*, 135–148. [[CrossRef](#)]
46. Han, J.; Tao, Z.; Xie, Y.; Liu, Q.; Shi, H. Radiometric cross-calibration of GF-4 satellite PMS sensor considering the characteristics of multiple integration times. *Acta Geod. Cartogr. Sin.* **2020**, *49*, 1311–1320.
47. Liu, J.; Li, Z.; Qiao, Y.; Liu, Y.; Zhang, Y. A new method for cross-calibration of two satellite sensors. *Int. J. Remote Sens.* **2004**, *25*, 5267–5281. [[CrossRef](#)]
48. Zhang, X.; Feng, R.; Li, X.; Shen, H.; Yuan, Z. Block adjustment-based radiometric normalization by considering global and local differences. *IEEE Geosci. Remote Sens. Lett.* **2022**, *19*, 8002805. [[CrossRef](#)]
49. Gao, C.; Jiang, X.; Ma, L.; Huo, H. Review of radiometric cross-calibration. *Arid. Land Geogr.* **2013**, *36*, 139–141.

Disclaimer/Publisher’s Note: The statements, opinions and data contained in all publications are solely those of the individual author(s) and contributor(s) and not of MDPI and/or the editor(s). MDPI and/or the editor(s) disclaim responsibility for any injury to people or property resulting from any ideas, methods, instructions or products referred to in the content.